

# Determination of Optimum Laser Surface Treatment Parameters of Plasma-Sprayed Yttria-Stabilized Zirconia Thermal Barrier Coatings

Ali AVCI<sup>1,\*</sup>, Muhammet KARABAŞ<sup>2</sup>, Ayşegül AKDOĞAN EKER<sup>3</sup>, Erhan AKMAN<sup>4</sup>, Caner ASLAN<sup>3</sup>

<sup>1</sup>Department of Mechanical Engineering, Hakkari University, Hakkari, Türkiye

<sup>2</sup>Department of Aeronautics and Astronautics, Kırklareli University, Kırklareli, Türkiye

<sup>3</sup>Department of Mechanical Engineering, Yıldız Technical University, Istanbul, Türkiye

<sup>4</sup>Department of Aeronautics and Astronautics, Kocaeli University, Kocaeli, Türkiye

*In this study, Yttria-stabilized zirconia (YSZ) thermal barrier coatings were fabricated by plasma spraying. The surface of the YSZ coatings was modified using a CO<sub>2</sub> laser to eliminate surface defects. Laser-glazed tracks were created on the coating surface with many different parameter variations to determine the optimum laser parameters. The microstructure of these tracks was examined by scanning electron microscopy. The optimum laser parameter was determined as 77.7 W laser power, 120 mm s<sup>-1</sup> scanning speed, and 215 mm laser distance according to microstructural properties. The optimization process showed that the laser parameters are effective on the glazed layer microstructure. After optimization work, a whole coating surface was glazed using optimum laser parameters. Structural characterization and hardness tests were applied to laser-glazed and unglazed coating in order to understand the effect of the laser glazing. Also, the fracture toughness of the laser-glazed layer was calculated. After laser glazing, a 30-50 µm thick, dense layer combined with a coating was obtained. A crack network formation was observed on the surface. Surface roughness decreased almost 10 times compared to unglazed YSZ. The monoclinic ZrO<sub>2</sub> phase in the coating structure was eliminated. The surface hardness and fracture toughness of the coating was improved after laser glazing.*

**Keywords:** Laser processing, YSZ, Fracture toughness, Microhardness, Thermal barrier coating

## Highlights:

- 77.7W laser power, 120 mm s<sup>-1</sup> scanning speed, and 215 mm laser distance were found as optimum laser parameters.
- For this purpose, 32 different laser parameters were applied to the YSZ coating surface. The optimum laser parameter was determined according to microstructure, the surface roughness, and the thickness of the laser glazing area which is confirmed by 30–50 µm, of the coating
- In addition, the surface hardness was increased by a factor of 3 and the fracture toughness of the coating was improved after the optimum laser glazing process.
- A dense layer with lower surface roughness and maximum surface depth was obtained by optimum laser processing parameters.

## 0 INTRODUCTION

The improvement of new coating materials provides an increasing the life of the high temperature exposed underlying substrate. Due to the gas turbine inlet temperature increasing day by day, the development of new and alternative TBCs materials which are continuously high-performance and durable coatings gained importance[1]. Blades and combustion chamber parts in the high-temperature region of gas turbine

engines are coated with ceramics with low thermal conductivity, high melting temperature and high thermal expansion in order to protect them from an aggressive environment. Thermal barrier coatings (TBC) are employed in different components such as gas turbines, marine engines, combustor chambers, power generation, pyrochemical reprocessing units and many more to protect their high temperature and to improve the efficiency of high temperatures in the working environmental [2], [3][4]. Turbine parts coated with TBCs not

\*Corr. Author's Address: Hakkari University, Keklikpinar Mh. Muhendislik Fakultesi, Hakkari, Türkiye,  
[aliavci@hakkari.edu.tr](mailto:aliavci@hakkari.edu.tr)

only provide thermal isolation under high thermal loads components but also provides higher engine efficiency, lower cooling requirements, and emission reduction [5]. Typical, thermal barrier coatings consist of three layers: a thermal isolation ceramic top layer, an intermediate thermally-grown oxide layer (TGO) and a metallic bond layer [4], [6]. Thin TGO which includes mainly the alumina layer consists of during operation temperature between bond-top coat interface since the oxygen passes from the surface through the bond coat [7]. The nickel-based metallic bond layer protects the substrate from oxidation [4], [8]. It also compensates for thermal expansion mismatches, which can cause thermal stress, cracks formation and failure of the TBCs system, between the ceramic top layer and the substrate [9]. 8 wt% yttria (8YSZ) is mostly used as a ceramic top layer due to its outstanding properties such as relatively high coefficient of thermal expansion ( $11 \times 10^{-6} \text{ K}^{-1}$ ) (1073 K) and low thermal conductivity ( $1.5$  to  $2.1 \text{ W m}^{-1} \text{ K}^{-1}$ ) low thermal conductivity [10]. In addition, properties such as high fracture toughness, phase stability at high temperatures, and high environmental corrosion resistance are expected from top-layer ceramics [11].

Yttria-stabilized zirconia (YSZ) thermal barrier coatings are most commonly produced by plasma spray [12]. In the plasma spray process, a plasma flame is created by using gas mixtures such as Ar/H/He. Spherical micron-sized powder feedstock material is fed into the plasma flame with the help of a powder feeder unit. Feedstock powder is sprayed toward the substrate in molten/semi-melt form. In-flight particles reaching the substrate are overlapped and bonded to each other. The bond layer is most commonly fabricated with high-velocity oxygen fuel (HVOF) due to it provides a lower particle temperature and a higher particle velocity compared to atmospheric plasma spray (APS) methods [13]. Therefore, HVOF has good adhesion to coatings, which have a lower content of oxides and lower porosity and higher deposition efficiency than APS methods [14]. Plasma-sprayed YSZ coatings include around 10-20% [15] porosity which contains a lot of a number of cracks and voids. Porosity provides, strain tolerance, isolation and segmentation crack stopper resulting in improving the lifetime of the TBC [16].

Laser surface modification can protect the coating against environmental effects by obtaining a dense and smooth layer on the surface without increasing the thermal conductivity of the coating and reducing the expansion tolerance. The top coat is quickly remelted to a depth of specific microns by a scanning laser beam using an advanced laser glazing process. Therefore, rapid resolidification within the modified depth inducts a controlled network of segmentation cracks and a dense layer. In order to obtain such a dense structure on the top layer, the researchers [15], [17]–[20] proposed laser glazing on the coating surfaces. To determine the durability and strain tolerance of the TBCs fracture toughness and stiffness are two basic properties under thermo-mechanical loading [21]. Reza et al. [2], [22] claim that laser surface modification provided a smoother surface and improved hardness properties by about 15% of the laser-glazed YSZ compared to unglazed YSZ. Morks et al. [2] as sprayed YSZ coating had lower Vickers hardness compared to laser glazed coating. They also reported that due to grain size decrease after laser glazing the hardness values of the YSZ increased. Due to the lower fracture toughness of the typical thermal spraying coatings, the inherent fracture toughness of the TBC is a significant phenome affecting the coating lifetime. [23] et al. studied the fracture toughness of the as-sprayed  $\text{La}_2\text{Ce}_2\text{O}_7/\text{YSZ}$  composite and  $\text{La}_2\text{Ce}_2\text{O}_7$  thermal barrier coatings. The addition of YSZ into  $\text{La}_2\text{Ce}_2\text{O}_7$  can cause improved fracture toughness due to a higher energy-relieving rate. Soleimanipour et al. [24] reported that laser glazing  $\text{Al}_2\text{O}_3/\text{ZrO}_2$  showed higher fracture toughness and thermal stability than unglazed composite since the existence of continuous network cracks perpendicular to the surface in the laser glazing layer. Thermal shock, thermal cycling and hot corrosion resistance of the TBCs increase due to laser glazing and also improve vertical cracks and voids thanks to rapid solidification [25]. Due to shrinkage during solidification cracks occur between splats in the coating. These microstructural properties inhibit thermal conductivity by reducing phonon scattering and provide thermal expansion tolerance [3], [26]. Besides these advantages, it brings a disadvantage in environmental-induced corrosion which occurs due to dust in the atmosphere entering through turbines and melting the TBCs in the hot region. In addition, Na, V, and S impurity

elements in the fuel accumulate on the coating surface over time. They react with yttria and cause destabilization which leads to accelerates the tetragonal-monoclinic phase transformation and volume expansion by about 5% [25]. Ghasemi et al. [27] reported that laser glazing reduced surface porosities and surface roughness of the thermal barrier coatings due to laser glazing improving the structural integrity. Calcium-magnesium-alumina-silicate (CMAS) infiltration from surface to bond coat significantly decreased after laser glazing of the as-sprayed YSZ [3]. Guo et. al [28] plasma-sprayed YSZ TBCs were subjected to hot corrosion after laser glazing. They reported that the amount of monoclinic phase formed as a result of destabilization decreased in laser-glazed YSZ compared to the untreated coating, as well as that the laser-glazed layer provided integrity against molten salt. However, they also reported that vertical cracks formed after laser glazing facilitate molten salt penetration and cause corrosion. Varghese et al. [29] found that laser remelting was applied to plasma-sprayed YSZ coatings against molten sodium corrosion. In their molten sodium corrosion experiments, they reported that vertical segmentation cracks formed as a result of laser remelting caused molten sodium penetration. They reported that molten sodium went down into the untreated area and diffused into the pavement through porosity and a network of cracks. Thus, desirable protection could not be achieved. According to these two studies, there is a need for a denser surface structure with a less vertical crack network for TBCs. This can be achieved by optimizing the laser process parameters. Milesan et al. [30] reported that CO<sub>2</sub> laser glazing presented low laser power values and low values of the roughness of the hard steel sheet.

There are many studies on the laser surface treatment [1]–[3], [5], [19], [20], [31]–[39] of the plasma sprayed thermal barrier coating. However, it was concluded that the study on finding the optimum laser parameter for the thermal barrier coating is very rare, even though there is no study

on the effect of the optimum laser parameter on the fracture toughness and hardness values of YSZ. For this reason, in this study, laser-glazed tracks with different laser distances (195 mm and 215mm), laser powers which are 28, 36.5, 44.6, 52.9 61.1, 69.4, 77.7, and 85.9 W, and scanning speeds which are 60, 80, 100, 120, 140, 160, 180 and 195 mm s<sup>-1</sup> were created using a CO<sub>2</sub> laser with various laser powers on the surface of plasma-sprayed YSZ TBCs. The cross-section and surface microstructures of these tracks were examined and the optimum laser surface modification parameters were determined. The whole coating surface was modified with the optimum parameters. The structural and mechanical properties of the whole surface-modified coating were also investigated.

## 1 METHODS and EXPERIMENTAL

### 1.1 Coating Deposition

Disc-shaped AISI 304 stainless steel coupons, which were cut by a laser cutting machine diameter of 25.4 mm and thicknesses of 3 mm, were used as a substrate. The substrates were grit blasted using 50-80 grain mesh alumina with a 200 mm gun distance to improve interface adhesion between substrate and bond coats and to remove possible ruins on the metallic surface. The substrates were stacked with double-way sticker tape to achieve homogeneous surface roughness on all sample surfaces. After grit blasting, the surface roughness of the substrate was measured as around 2.7 μm [40] with an optical profilometer (Veeco WYKO NT1100) device. The samples were cleaned using an ultrasonic cleaning device in ethanol for 30 min before bond coat deposition. Grit-blasted samples were clamped to a rotating table at 100 revolutions per min (rpm) for 12 passes. Metco AMDRY 997 commercial powder was deposited on the samples by the HVOF spraying method as a bond coat. Table 1 shows the HVOF process parameters.

**Table 1.** Process parameters of HVOF

Material	Pressure (bar)			Flow Rate (SCFH)			Process	
	Oxygen	Propane	Air	Oxygen	Propane	Air	Spray distance	Feeding rate
Amdry 997	10.3	6.2	7.2	24	40	50	250 mm	50 g min <sup>-1</sup>

After bond coat deposition, the ceramic top coat, whose commercial name is Metco 204B-NS YSZ ( $ZrO_2-8 \text{ wt.}\%Y_2O_3$ ), was deposited using the atmospheric plasma spraying technique. Table 2 illustrates the APS process parameters. The gun nozzle selected was a commercial 9MBM with a powder injection angle perpendicular to the plasma flame.

**Table 2.** Process parameters of plasma spray

Parameters	
Current (A)	5500
Primary gas flow rate, Ar (scfh)	990
Secondary gas flow rate, H <sub>2</sub> (scfh)	115
Carrier gas flow rate, Ar (scfh)	113.5
Number of passes	112
Spray distance (mm)	775
Gun speed (mm/min)	6600
Turntable speed (rpm)	1100

### 1.2 Laser Surface Modification

The surface treatment was carried out using a pulsed CO<sub>2</sub> laser. This laser operated at a 10.6  $\mu\text{m}$  wavelength with a pulse duration in the range of 5–400  $\mu\text{s}$  and a repetition rate range between 5 kHz and 100 kHz. A galvanometric system that provides the computer-controlled movement of the laser beam was used with a 160 mm focal length F-Theta lens, to achieve desired surface area. The parameters include laser power, scanning speed, fill spacing (distance between subsequent laser tracks), the distance between the F-Theta lens and

**Table 3.** Laser processing parameters

	Materials	Laser Distance	Laser Power	Scanning Speed
Parameters	YSZ	215 mm	28 W	60 mm s <sup>-1</sup>
			36.5 W	80 mm s <sup>-1</sup>
			44.6 W	100 mm s <sup>-1</sup>
			52.9 W	120 mm s <sup>-1</sup>
			61.1 W	140 mm s <sup>-1</sup>
		195 mm	69.4 W	160 mm s <sup>-1</sup>
			77.7 W	180 mm s <sup>-1</sup>
			85.9 W	195 mm s <sup>-1</sup>

### 1.3 Characterization Studies

APS YSZ and laser-glazed YSZ TBCs were examined by scanning electron microscopy (Phenom-World XL) from the cross-section and surface of the coating. Physical properties such as dense layer microstructure, the thickness of the

the samples, and the pulsed frequency. The software controlling the laser device (Ezcad) uses Pulse Width Modulation (PWM) signals and the power increase is provided by percentage increments in the software. For this reason, laser glazing processing was performed in 2% increments made in the software, which corresponds to 8W laser power in the processing region in our experimental setup. Since the percentile expression in the laser control software is a relative parameter, the power values are given in the text because it is thought that the values measured with a power meter in the processing area are more useful. In order to determine the optimum parameters, various scanning speeds, distances and laser power were investigated as seen the Table 3. The surface and cross-section characterization of the obtained laser scan traces were provided and the laser parameters were optimized in line with the determined target criteria. As a result of laser scans, thirty-two different scan traces were obtained on the surface of the YSZ coating. The optimum laser parameter was determined according to microstructure, the surface roughness and the thickness of the laser glazing area which is confirmed by 30–50  $\mu\text{m}$  [2], [41]. In the laser glazing, samples were tried to be processed with equal increases in laser power by determining the lower limit where the laser power has a minimum effect and the upper limit causing the spallation of the coating.

coatings and porosity were achieved as a result of laser glazing using the SEM device. The porosity results were obtained from the SEM images of both the cross-sectional and surface of the YSZ coatings according to ASTM-B276. Surface roughness values of the coatings were measured

using a stereographic option which captured pictures of the TBC from different angles of the SEM device. Thus, a 3D model of the coating surface obtains from the SEM pictures of the coating with 10 nm precision. Surface roughness measurements were applied five times for four random places on the sample surface. The average surface roughness was found by drawing 5 different lines from each surface for porosity measurements. Afterward, this process was repeated in 4 different parts of the surface and the results were obtained from 20 different. Microhardness measurement was conducted on the whole surface of glazed samples with a load of 500 g (4.9 N) for 25 seconds. Hardness tracks and formulation possible cracks were observed through not only light microscopy but also SEM device. The following equation can be used to find out the surface fracture toughness of the coating after the optimum laser parameter [42], [43];

$$K_{IC} = 0.16\left(\frac{c}{a}\right)^{-1.5}(Ha^{1/2}), H=1.8P a^{-2} \quad (1)$$

where  $K_{IC}$  is fracture toughness ( $\text{MPa}\cdot\text{m}^{1/2}$ );  $H$  is Vickers hardness (MPa);  $P$  is test load in Vickers hardness (MPa);  $c$  is the average length of the cracks obtained in the tips of the Vickers marks ( $\text{m}\mu$ ), and  $a$  is the half average length of the diagonal of the Vickers marks ( $\text{m}\mu$ ).

X-ray diffraction characterization of the YSZ powder, the as-sprayed coating, and the laser-glazed coating was conducted by parameters at  $2\Theta=10-90^\circ$  and  $5^\circ \text{min}^{-1}$  scanning speed. The wt% phase fraction of the monoclinic  $\text{ZrO}_2$  phase ( $X_m$ ) was calculated by using peak intensities in the range of  $2\Theta=28-32^\circ$ . Eq. (2) was used for calculation [43].

$$X_m = \frac{I(11\bar{1})_m + I(111)_m}{I(11\bar{1})_m + I(111)_m + I(111)_{c,t}} \quad (2)$$

Besides, the wt% fraction of cubic phase ( $X_c$ ) was calculated by peak intensity of cubic (400) peak, tetragonal (400) and (004) peak in the range of  $2\Theta=72-76^\circ$ . Eq (3) was used in the calculation [44].

$$X_m = \frac{I(400)_c}{I(004)_t + I(400)_t + I(400)_c} \quad (3)$$

## 2 RESULTS AND DISCUSSIONS

### 2.1 Coating Characterization

Fig. 1 shows cross-sectional and surfaces SEM images of the as-sprayed YSZ coating, respectively. Fig. 1 a) shows a typical thermal barrier coating which consists of a substrate, NiCoCrAlY bond layer coated on the substrate and YSZ top coat deposited on the bond coat. Fig. 1 b) presents a cross-sectional SEM image of the YSZ with lamellar microstructure and columnar-grain splats. SEM images also show continuous adhesion between the bond coat-top coat and bond coat-substrate. It is seen from Fig. 1 that the bond coat thickness is around 70–85  $\mu\text{m}$  and the YSZ top coat has 210–225  $\mu\text{m}$  thickness. Fig. 1 shows the surface microstructure of YSZ TBC after coating deposition with many defects which makes the top coat very rough, such as porosity, cracks, partially molten powders, and splats formed during the solidification of melted powders. Un-molten and partially molten YSZ particles make weakly bond to each other, resulting they cause occurring a porous microstructure in the coating. In contrast, the top layer bond coat has a dense and non-porous structure because of the HVOF method. The YSZ top layer is in the traditional plasma-sprayed coating microstructure.

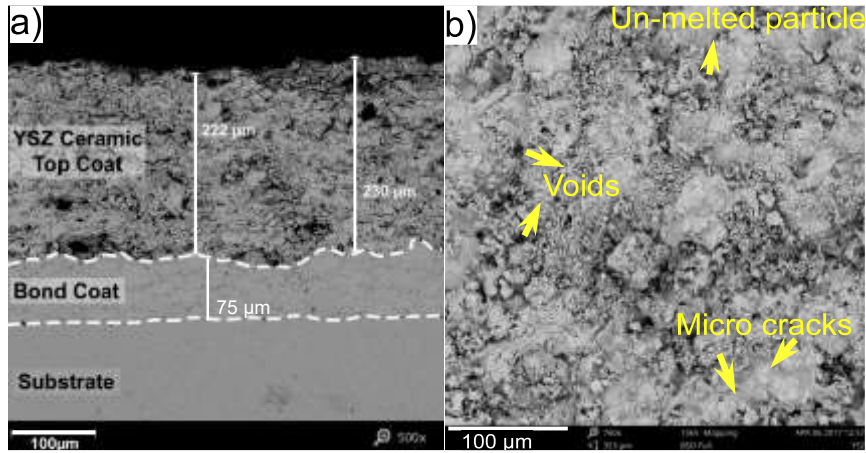
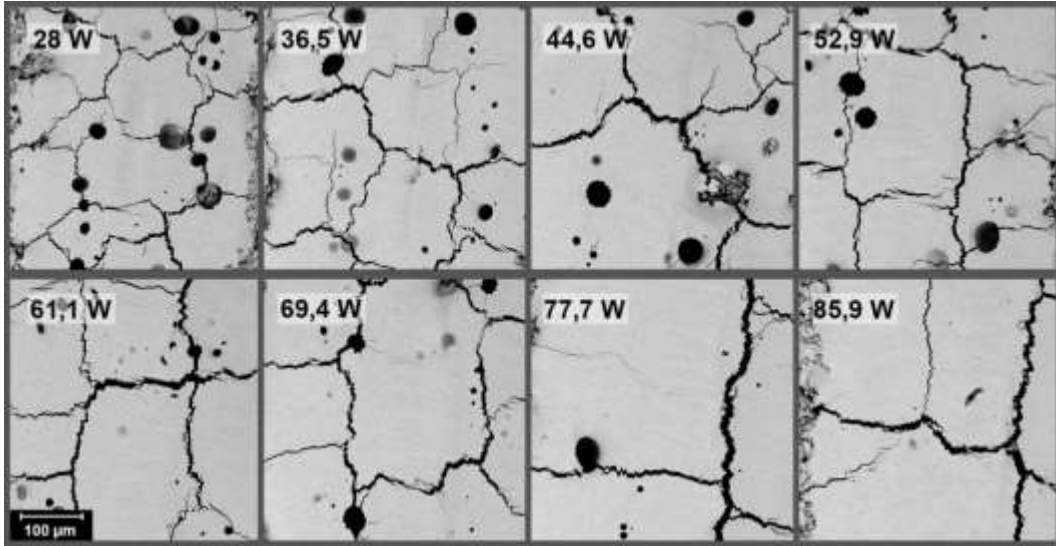


Fig. 1. The SEM images of YSZ TBCs, a) Cross-sectional image, b) Surface image

## 2.2 Characterization of Laser Remelted Coatings

Surface SEM images of laser tracks were achieved by using a constant scanning speed ( $120 \text{ mm s}^{-1}$ ) and laser distance (215 mm) however, gradually increasing laser power is shown in Fig. 2. Compared to the initial surface structure, the surface microstructure of the coatings changed a lot as a result of laser glazing. Grain forming of laser glazed surface consists of three stages, which are heating, melting, and solidification. When the laser beam is absorbed by the coating surface, the surface temperature quickly goes up and begins to melt. After that, the melted areas begin to re-solidified, which is also the fine grains forming step, immediately following the onward laser light [2]. A flat surface is formed, and there is a continuous crack network formation on all surfaces. These cracked networks may cause shrinkage and increase in density on the coating surface as a result of rapid solidification during laser glazing [29], [45]. As a result of the increase in laser power, the area of the region limited by the cracks extended. It has been seen in Fig. 2 the size

of the gap between the two cracks increased. It is seen the Fig. 2 that the 69.4 W, 77.7 W and 85.9 W laser powers applied surfaces have continuous surface areas and their roughness is lower than the others. The best surface result was obtained when 77.7 W laser power was applied to the surface. Melting increased with the growth of heat energy input to the coating surface. The increase in melting causes a greater volume of coating to be melted. For this reason, larger islets and inter-islet gaps are formed as you see in Fig.2. In addition, crater-like depressions are randomly distributed on the surface. These cavities are formed as a result of gases rising to the surface, which were trapped in the porosities during insufficient melting and solidification during coating production. In the plasma spraying process, overlapping of unmelted and semi-molten particles creates porosities. Due to unmelted particles being melted as a result of energy input to the porous area, the porosity is filled with gas. Rapid solidification leads to trapping gas inside the coating resulting in, crater-like structures formed on the laser-glazed surface [36].



**Fig. 2.** SEM surface images of the laser tracks were obtained by increasing laser power gradually from 28 W to 85.9 W, laser distance at 215 mm, scanning speed in 120 mm s<sup>-1</sup> for YSZ coating

When the laser distance was decreased by 195 mm keeping the scanning speed constant, partial melting occurs on the surface at the lowest power. There are pits on the surface resembling the initial microstructure. By increasing the laser power, a flatter surface has begun to be obtained. As in the first experiment, the increase in laser power caused an increase in the area of the crack islets and an increase in the gaps between the islets. Crater formation increased with the approaching laser distance. In summary, the melting increased with the increase in laser power. This resulted in greater enlargement of the crack islets and increased solidification shrinkage. Thus, the distance between the islets increased. This means more gaps in the coating surface for CMAS and hot corrosion salts to fill. It also creates gaps for environmental corrosives in crater-like depressions. For this reason, the effect of scanning speed was investigated for obtaining a flatter surface. The microstructures of the tracks were obtained by increasing the scanning speed at constant laser power and laser distance.

When the scanning speeds increased from 60 mm s<sup>-1</sup> to 200 mm s<sup>-1</sup> at 215 mm laser distance and 28 W laser power, SEM surface images of laser tracks showed the crack islets decreased in size. The crack spacing between islets also decreased. The energy input during glazing

decreased with the increase in scanning speed. The number of crater-like depressions also increased. Experiments were continued by reducing the laser distance to 195 mm with an increase in scanning speed the melting of the coating surface decreased. Sections reminiscent of the initial coating microstructure can be seen in the tracks obtained at 140 and 160 mm s<sup>-1</sup> speeds. This indicates that sufficient melting did not occur at these speeds. At other speeds, a smoother surface was obtained. However, smaller crack islands were formed at a speed of 80 mm s<sup>-1</sup>. The less crater-like depressions mainly formed at 100 mm s<sup>-1</sup>.

In this section, the change in the surface microstructure was investigated as a result of decreased laser distance and increased scanning speed. Results show that a reduction in the laser distance and increasing in the scanning speed caused a reduction in the melting of the surface. The only surface microstructure is not sufficient to determine the optimum laser parameter. It is necessary to obtain a dense laser-glazed layer, which is not separated from the coating layer as well. For this reason, cross-sectional microstructures of all laser tracks were also examined. Fig. 3 shows cross-sectional SEM images of the laser tracks obtained by increasing the laser distance to 215 mm, scanning speed to 120 mm s<sup>-1</sup>, and laser power gradually from 28 W to 85.9 W. A dense layer was formed on all laser-glazed tracks that did not separate from the coating

layer. Laser-glazed layer thicknesses are close to one another. The laser-glazed layer thickness obtained with 28, 36.5, and 44.6 W laser power is thinner than the tracks produced at other laser powers. A dense layer of 20  $\mu\text{m}$  thick was obtained at these laser powers. In other powers, the laser-glazed dense layer thickness was measured at around 30  $\mu\text{m}$ . As seen the Fig. 3, when applied to

69.4 W, 77.7 W and 85.9 W laser powers at 120  $\text{mm s}^{-1}$  scanning speed with a laser distance of 215 mm continuous and thicker dense layers were achieved. A laser-glazed sample with 77.7 W laser power was selected as the best sample since its surface properties were better than the others as well.

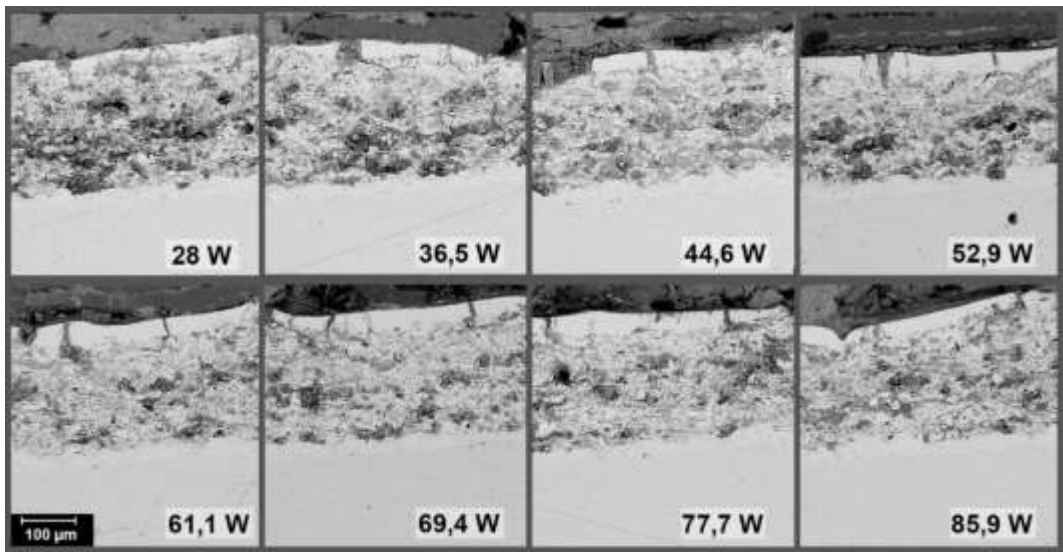


**Fig. 3.** Cross-sectional SEM images of the laser tracks were obtained by increasing the laser distance to 215 mm, scanning speed to 120  $\text{mm s}^{-1}$ , and laser power gradually from 28 W to 85.9 W

When SEM images of the laser tracks were obtained by reducing the laser distance to 195 mm, scanning speed to 120  $\text{mm s}^{-1}$ , and laser power gradually from 28 W to 85.9 W, the melting depth was reduced with the decrease in the laser distance. The layer thickness obtained with 215 mm laser distance decreased by half. However, the laser-glazed layer thickness increased with the increase in laser power. Especially at low powers such as 28 and 36.5, almost no dense layer was formed. A more distinct dense layer was formed on the tracks made with subsequent laser powers. At these powers, the layer thickness is 10-15  $\mu\text{m}$ . Laser power density decreased by decreasing the laser distance from 215 mm to 195 mm. This resulted in an inability to perform an effective glazing process. At all distances, there is a dense layer integrated with the coating. The thickness of this dense laser-glazed layer decreased with increased scanning speed.

### 2.3 Characterization of the laser-glazed coating using hardness, fracture toughness and XRD

In the previous section, optimum laser parameters were selected according to microstructure properties such as porosity, surface roughness, and acting laser glazing depth. While selecting the optimum laser parameter, microstructure changes, the laser acts depth and the formation of cracks on the thermal barrier coatings were determined as boundary conditions. While selecting the optimum laser parameter, attention was paid to ensuring that the laser depth was between 30-50  $\mu\text{m}$ . In the other words, the optimum parameter was achieved until the laser-glazed layer to being dense, integrated with the coating, had low surface roughness, and less crack network of 30-50  $\mu\text{m}$ . For this purpose, 32 different laser parameters were applied to the YSZ coating surface step by step to determine better microstructure in boundary conditions. The whole

surface of the APS YSZ was modified by laser under the most suitable parameters which are 77.7 W laser power, 120 mm s<sup>-1</sup> scanning speed, and 215 mm laser distance, determined after the optimization processes. Fig. 4 a) shows the laser glazed coating cross-sectional SEM image and Fig. 4 b) presents the surface microstructure SEM image of the full surface laser glazing with the optimum laser parameters which are 77.7 W laser power, 120 mm s<sup>-1</sup> scanning speed, and 215 mm laser distance. In the cross-section microstructure of the APS YSZ, a dense layer between 30-50 μm thick, integrated with the coating, was obtained. On the surface, there are wider cracked and narrower islets. However, there are areas where the

inter-crack distance is larger and crater-like depressions are absent on the laser-glazed YSZ surface.

Table 4 shows, the Ra surface roughness value measured as 5.26 μm and 0.69 μm before laser glazing, respectively. The Rz value of APS YSZ was 20.11 and laser-glazed YSZ was measured as 4.57 μm. The measured values prove that a flatter and smoother surface is achieved as a result of laser glazing. This reduction can be explained by, laser glazing providing dense and refined microstructure due to pores, cracks and voids which are come from the natural structure of the APS YSZ, which turned into a monolithic and dense structure.

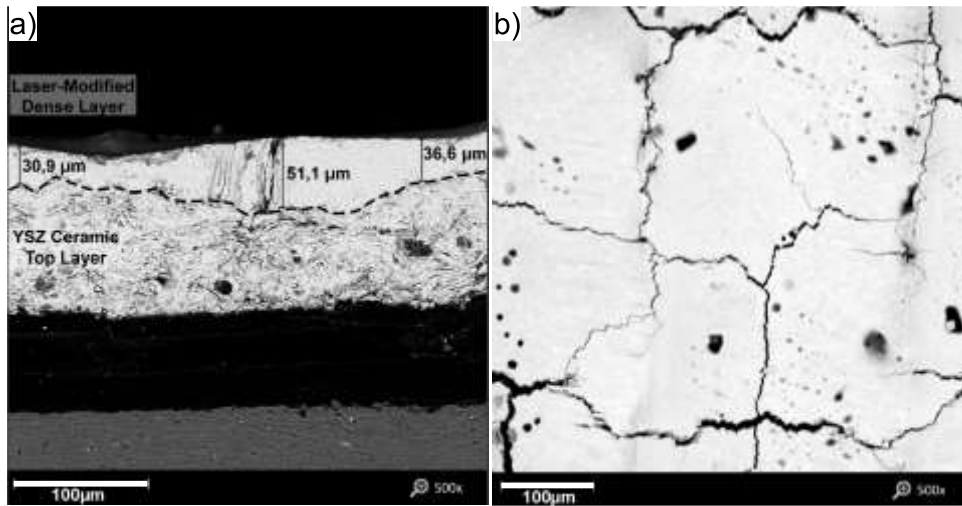


**Fig. 4.** a) Cross-sectional and b) surface SEM images of the YSZ coating in which full surface scanning was performed with 77.7W laser power, 120 mm s<sup>-1</sup> scanning speed, and 215 mm laser distance parameters

**Table 4.** Physical properties of conventional and laser-glazed YSZ TBC

Samples	Ra, Surface roughness (μm)	Rz, Max. surface depth (μm)	Microhardness (HV)	Fracture toughness (MPa m <sup>1/2</sup> )	Porosity (%)
Conventional YSZ	5.26 μm	20.11	985.8	1.83-2.24 [40]	13
Laser glazed YSZ	0.69	4.57	2813.8	7.4	5

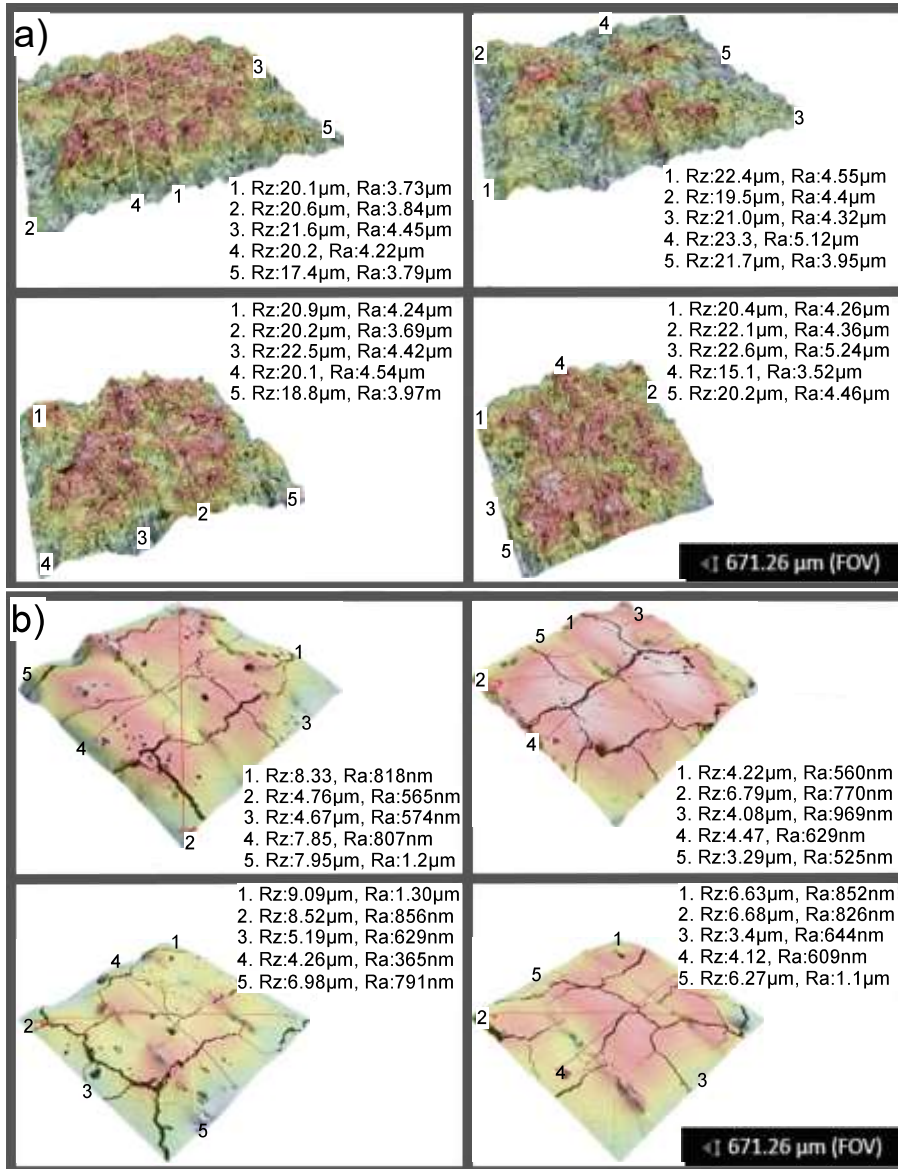


**Fig.5.** Surface roughness measurement in the different parts of the YSZ coatings; a) As sprayed YSZ, b) Laser glazed YSZ coating with optimum parameter

In previous studies [43], [46] reducing the surface roughness provides an advantage against damage mechanisms such as hot corrosion and molten CMAS due to the specific surface area of TBC decrease. As seen in Fig. 5, the fluctuation existing in the coatings before laser glazing significantly decreased after laser glazing. Blue and gray areas symbolize valleys and decreasing roughness values and the red areas symbolize peaks and increasing roughness values of the coating in Fig 5. APS YSZ coating SEM image includes porosity and splat formation which are

created during the plasma spray process. While the highest average surface roughness (Ra) of the APS YSZ is 5.24 μm, after laser glazing the value is reduced by 525 nm. A similar reduction was observed at the distance between the peaks and valleys of the sampled line in the y-direction (Rz) values. As the highest Rz value of the APS YSZ was measured at 23.32 μm, after laser glazing the lowest Rz value was found at 2.46 μm. It is understood the results of laser glazing remarkably reduced both Ra and Rz values of the APS YSZ. Paksereshtet al.[47] reported that reducing the

specific surface area and the surface roughness provides decreasing molten salt diffusion during a hot corrosion environment thereby the lifetime of the laser-glazed TBC is extended. CMAS corrosion is one of the significant damage mechanisms for thermal barrier coating. Guo et al. [48] claim that decreasing the surface roughness of the TBC improved the CMAS corrosion resistance. In addition, the natural lamellar stacking microstructure with high porosity of the APS YSZ was substantially erased after laser remelting. In a similar study, Wang et al. [49] found that laser-glazed TBC has better solid particle erosion and microhardness resistance than APS TBC. Table 4 shows the surface microhardness hardness values of APS YSZ and laser-glazed YSZ were measured as 985.8 and 2813.8 HV, respectively. Results showed that the microhardness of the APS YSZ increased by about 3 times compared to laser-glazed YSZ. It can be explained by during melting and rapid solidification in the laser processing, porosity and cracks were eliminated between splats. The fine-grained structure with many grain boundaries creates after laser glazing, leading to stopping dislocation propagation during plastic deformation. In the other words, grain boundaries absorb the existing energy therefore crack propagation reduces in the coating. By obtaining a fine-grained surface structure by laser, the surface hardness value increases [19]. Fig. 6 shows optical microscope images, crack propagation of the indentation zone and microstructure of the laser-modified coating. As seen the Fig. 6 the half average length of the diagonal of the Vickers and crack length was shown following letters "a" and "c", respectively. Fig. 6 also demonstrated a close view of the dense and fine grains microstructure of laser-glazed YSZ coating. Table 4 also shows the fracture toughness values of the laser-glazed and unglazed YSZ. The fracture toughness value of the laser-glazed surface was calculated as  $7.4 \text{ MPa m}^{1/2}$ . In previous studies, fracture toughness values for bulk YSZ and plasma-sprayed YSZ were reported as  $9.5 \text{ MPa m}^{1/2}$  [34] and  $1.83\text{-}2.24 \text{ MPa m}^{1/2}$  [40], respectively. When these values are taken as a reference, the fracture toughness value of the laser-glazed coating increased like hardness values since the fracture toughness and hardness have a direct relationship with each other's [24]. As discussed before, plasma-sprayed YSZ contains defects such as porosity and intersplat

cracking might promote crack propagation. Fracture toughness has been improved as a result of eliminating these defects on the surface and cross-section of the coating by laser. According to X-ray crystallography (XRD) results, monoclinic YSZ turned into a tetragonal YSZ phase.  $t'$  8YSZ has generally higher fracture toughness and hardness than cubic YSZ at room temperature due to ferroelastic toughening [19]. This phase can be explained by the change into monoclinic YSZ and the allotropic phase transformation of YSZ [23]. In addition, grains formed during laser glazing are also effective in improving fracture toughness. Fan et al. [50] reported that during laser glazing high cooling and solidification rate supports forming a columnar grain and fine microstructure which provides better fracture toughness and strain tolerance for TBCs.

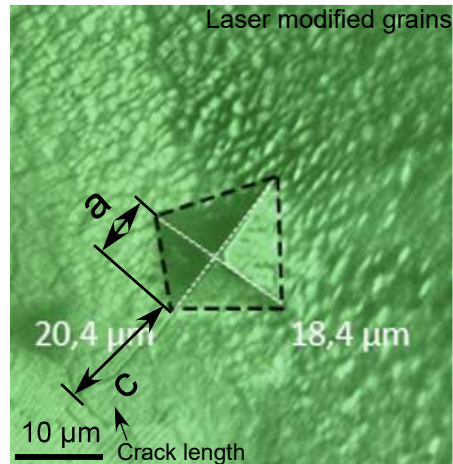


Fig. 6. Optical microscope image Vickers indentation zone and crack length

Fig. 7 shows XRD patterns of a) YSZ powder, b) plasma sprayed coating and c) laser-glazed coatings. Commercial YSZ powder contains two phases, tetragonal  $\text{ZrO}_2$ , and monoclinic  $\text{ZrO}_2$ . A little amount of monoclinic phase ( $m\text{-ZrO}_2$ ) was detected in the powder. The intensity of the tetragonal peaks is quite higher than the monoclinic phase. No phase transformation occurred in YSZ after plasma spraying. As in powder, monoclinic  $\text{ZrO}_2$  peaks are present in the structure at low intensities. However, after laser glazing, monoclinic  $\text{ZrO}_2$  peaks disappeared. With the energy input to the surface during laser glazing, the chemical composition of the regions containing the monoclinic and tetragonal phases becomes

homogeneous. The monoclinic phase without yttrium reacts with the Tetragonal phase containing yttrium. Thus, with the rapid cooling effect, the monoclinic phase transforms into the tetragonal phase [39]. Porosities and intersplat cracks are visible. The top layer contains about 13% porosity. The surface roughness values of the YSZ coating are given in Table 4. The average Ra value is 5.26  $\mu\text{m}$ , and the Rz value is 20.11  $\mu\text{m}$ . Ra values are close to the values in Nikhil R. Kadam's study [51].

According to the monoclinic phase, calculation results; YSZ powder feedstock contains 14 wt%, as-sprayed coating 18 wt% and laser glazed coating 3 wt% monoclinic phase. As a result of exposure of YSZ powder particles to high plasma temperature, the amount of monoclinic phase in the structure would be increased. During laser processing, the double-phase structure became homogeneous as a result of the sudden high energy input and rapid cooling of the structure. Thus, the percentage of the monoclinic

phase decreased drastically [39]. According to the calculations of the percentage of cubic phase in the structure, YSZ feedstock includes 25 %wt, as-sprayed coating 53% wt and laser glazed coating 38%wt cubic phase. Osorio et al. [52] found similar results of the sprayed YSZ coating. The percentage of cubic phase in the structure decreased after laser processing since the crystal orientation changed during laser glazing which can cause to rearrange of the coating microstructure. The lamellar structure turns into a columnar structure. The unmelted, semi-molten particles on the coating surface are cleaned by laser glazing. Thus, the cubic and non-cubic phase distribution changed as well [39]. Moreover, plasma spray parameters, feedstock powder type,  $\text{Y}_2\text{O}_3$  content, etc. are very effective on the phase fraction of the coatings. The amount of semi-molten, unmelted particles in the structure determines the fraction of the coating phase structure [53], [54].

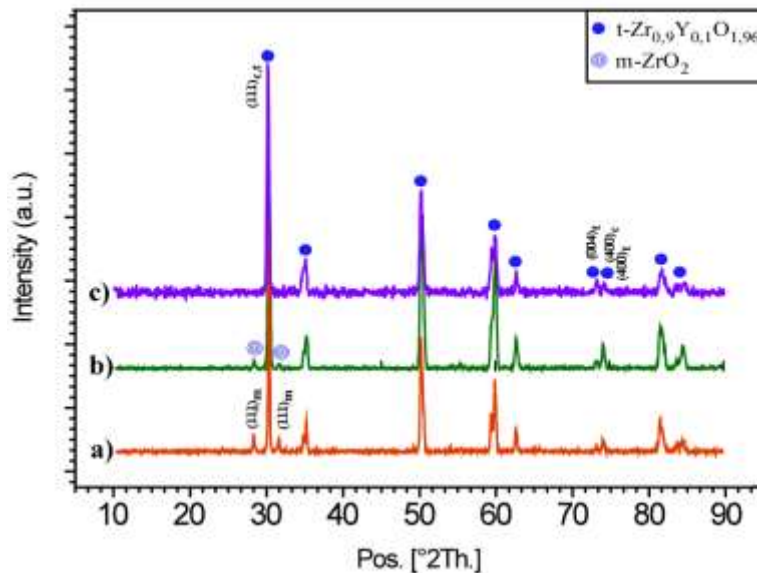


Fig. 7. XRD patterns of a) YSZ powder, b) as-sprayed YSZ coating, c) whole surface laser-glazed YSZ

### 3 CONCLUSIONS

In this study, laser surface modification parameters were optimized for plasma-sprayed YSZ TBCs. The whole surface was glazed with the experimentally determined most suitable

parameters. Briefly, the following conclusions can be drawn;

- The optimum parameter was determined as 77.7 W laser power, 120 mm s<sup>-1</sup> scanning speed, and 215 mm laser distance for YSZ TBCs.
- When the laser power and laser distance were increased, the melting depth reduced.

- As energy input reduced from 85.9 W to 28 W the melting thickness decreased resulting in microcracked islets and crater-like pits formed.
- A dense layer with lower surface roughness and maximum surface depth was obtained by optimum laser processing parameters.
- In addition, the surface hardness was increased by a factor of 3 and the fracture toughness of the coating was improved after the optimum laser glazing process.
- The residual monoclinic phase in the coating structure was eliminated by laser glazing.

Although laser surface modification eliminates surface defects of TBCs, the formation of a crack network is disadvantageous for glassy deposit and hot corrosion mechanisms. In further studies, the crack network on the surface could be filled with nanoscale processes.

#### 4 ACKNOWLEDGEMENTS

Scientific Research Project Fund of Yildiz Technical University, Project Number FBA-2017-3057. The authors would like to thank the Yildiz Technical University Scientific Research Project Coordination Department for financial support.

#### 5 NOMENCLATURES

$K_{IC}$	[MPa·m <sup>1/2</sup> ] Fracture toughness
H	[MPa] Hardness Vickers
P	[N] Test load
$R_a$	[µm] Average surface roughness
$R_z$	[µm] Distance between the peaks and valleys

#### 6 REFERENCES

[1] Zhang, P., Sun, L., Zhang, X., Wang, Y., Zhang, Q., Yao, J. and Chang F. (2021). Thermal cycling behavior of selective laser remelted thermal barrier coatings with different laser dot distances. *Journal of Thermal Spray Technology*, vol. 30, no. 4, p. 1038–1048, DOI:10.1007/S11666-021-01173-3/figures/11.

[2] Morks, M. F., Berndt, C. C., Durandet, Y., Brandt, M and Wang, J. (2010). Microscopic observation of laser glazed yttria-stabilized zirconia coatings. *Appl Surf Sci*, vol. 256, no.

21, p. 6213–6218, DOI:10.1016/J.apsusc.2010.03.143.

[3] Bakkar, S., Pantawane, M.V., Gu, J.J., Ghoshal, A., Walock, M., Murugan, M., Young, M.L., Dahotre, N., Berman, D., Aouadi, S.M. (2020). Laser surface modification of porous yttria stabilized zirconia against CMAS degradation. *Ceram Int*, vol. 46, no. 5, p. 6038–6045, DOI:10.1016/J.ceramint.2019.11.061.

[4] Savin, A., Craus, M.L., Turchenko V., Novy, F., Mocanu A.C., Soare, M., Grum, F., Doroshkevich, O.S. (2018). Complementary methods for evaluation of yttria stabilized zirconia coatings used as thermal barrier coating. *Strojniški Vestnik/ Journal of Mechanical Engineering*, vol. 64, no. 11, p. 706–715, DOI: 10.5545/SV-JME.2017.5107.

[5] Khan, M. A., Anand, A. V., Duraiselvam, M., Rao, K. S., Singh, R. A. and Jayalakshmi, S. (2021). Thermal shock resistance and thermal insulation capability of laser-glazed functionally graded lanthanum magnesium hexaluminate/yttria-stabilised zirconia thermal barrier coating. *Materials*, vol. 14, no. 14, p. 3865, DOI: 10.3390/MA14143865.

[6] Avci, A., Eker, A. A., Eker, B. (2018). Microstructure and oxidation behavior of atmospheric plasma-sprayed thermal barrier coatings. *Exergetic, Energetic and Environmental Dimensions*, p. 793–814, DOI: 10.1016/B978-0-12-813734-5.00045-7.

[7] Arshad, A., Yajid, M. A. M., Idris, M. H. (2021). Microstructural characterization of modified plasma spray LZ/YSZ thermal barrier coating by laser glazing. *Mater Today Proc*, vol. 39, p. 941–946, DOI:10.1016/J.matpr.2020.04.145.

[8] Naumenko, D., Pillai, R., Chyrkin, A., Quadackers, W. J. (2017). Overview on recent developments of bondcoats for plasma-sprayed thermal barrier coatings. *Journal of Thermal Spray Technology*, vol. 26, no. 8, p. 1743–1757, DOI: 10.1007/S11666-017-0649-Z/figures/16.

[9] Wang, X., Bai, X., Xiao, W., Liu, Y., Li, X., Wang, J., Peng, C., Wang, L., Wang, X. (2022). Calculation of thermal expansion coefficient of rare earth zirconate system at high temperature by first principles. *Materials (Basel)*, vol. 15, no. 6, DOI:10.3390/MA15062264.

[10] Thakare, J. G., Pandey, C., Mahapatra, M. M., Mulik, R. S. (2020). Thermal barrier coatings—

- A State of the Art Review. *Metals and Materials International*, vol. 27, no. 7, p. 1947–1968, DOI:10.1007/S12540-020-00705-W.
- [11] Tenango-Pirin O., Reynoso-Jardón, E., García, J.C., Mariaca, Y., Hernández, Y.S., Neco R., Dávalos O. (2020). Effect of thermal barrier coating on the thermal stress of gas microturbine blades and nozzles. *Strojniški Vestnik/Journal of Mechanical Engineering*, vol. 66, no. 10, p. 581–590, DOI: 10.5545/SV-JME.2020.6883.
- [12] Łatka, L., Pawłowski, L., Winnicki, M., Sokołowski, P., Małachowska, A., Kozerski, S. Review of functionally graded thermal sprayed coatings. *Applied Sciences*, vol. 10, no. 15, p. 5153, DOI: 10.3390/app10155153.
- [13] Fauchais, P. L. Heberlein, J. V. R., Boulos, M. I. (2014). Thermal spray fundamentals: From powder to part. *Thermal Spray Fundamentals: From Powder to Part*, p. 1–1566, DOI:10.1007/978-0-387-68991-3/cover.
- [14] Lima, R. S. (2022). Porous APS YSZ TBC manufactured at high powder feed rate (100 g/min) and deposition efficiency (70%): microstructure, bond strength and thermal gradients. *Journal of Thermal Spray Technology*, vol. 31, no. 3, p. 396–414, DOI:10.1007/S11666-021-01302-Y/Figures/10.
- [15] Tillmann, W., Khalil, O., Baumann, I. (2021). Influence of direct splat-affecting parameters on the splat-type distribution, porosity, and density of segmentation cracks in plasma-sprayed ysz coatings. *Journal of Thermal Spray Technology*, vol. 30, no. 4, p. 1015–1027, DOI:10.1007/S11666-021-01180-4/figures/10.
- [16] Karabas, M., Bal, E., Taptik, Y. (2016). Effect of air plasma spray parameters on the properties of YSZ and CYSZ thermal barrier coatings. *Journal of the Australian Ceramic Society*, vol. 52 no.2, p.175-182.
- [17] Chen, H.F., Zhang, C., Liu, Y.C., Song, P., Li, W.x., Yang, G., Liu, B. (2019). Recent progress in thermal/environmental barrier coatings and their corrosion resistance. *Rare Metals*, vol. 39, no. 5, p. 498–512, DOI: 10.1007/S12598-019-01307-1.
- [18] Park, K. Y., Jang, K. I., Myoung, S. W., Jung, Y. G., Yang, B., Kim, J. S. (2021). Degradation characteristics of thermal barrier coatings for hot corrosion and CaO–MgO–Al<sub>2</sub>O<sub>3</sub>–SiO<sub>2</sub>. *Surf Coat Technol*, vol. 412, no.1, p. 127045, DOI:10.1016/J.surfcoat.2021.127045.
- [19] Kumar, V. Verma, R., Kango, S., Sharma, V. S. (2021). Recent progresses and applications in laser-based surface texturing systems,” *Mater Today Commun*, vol. 26, p. 101736, DOI:10.1016/J.mtcomm.2020.101736.
- [20] Li, W.; Li, Z.; An, G.; Cheng, B.; Song, Q.; Sun, J.; Vaganov, V.; Wang, C.; Goransky, G. (2022). Isothermal oxidation tgo growth behaviors of laser-remolten lzo/ysz thermal barrier coatings. *Coatings*, vol. 12, no. 2, p. 107, DOI:10.3390/coatings12020107.
- [21] Wang, Y., Darut, G., Luo, X.T., Poirier, T., Stella, J., Liao, H., Planche, M.P. (2017). Influence of preheating processes on the microstructure of laser glazed YSZ coatings. *Ceram Int*, vol. 43, no. 5, p. 4606–4611, DOI:10.1016/J.ceramint.2016.12.125.
- [22] Reza, M. S., Aqida, S. N., Mohd M. R. (2014). An investigation of phase crystallinity in laser modified yttria stabilized zirconia (YSZ) thermal barrier coating. *Key Eng Mater*, vol. 611–612, p. 1601–1607, DOI:10.4028/www.scientific.net/kem.611-612.1601.
- [23] Dehkharghani, A. M. F., Rahimipour, M. R., Zakeri, M. (2020). Improving the thermal shock resistance and fracture toughness of synthesized La<sub>2</sub>Ce<sub>2</sub>O<sub>7</sub> thermal barrier coatings through formation of La<sub>2</sub>Ce<sub>2</sub>O<sub>7</sub>/YSZ composite coating via air plasma spraying. *Surf Coat Technol*, vol. 399, p. 126174, DOI:10.1016/J.surfcoat.2020.126174.
- [24] Soleimanipour, Z., Baghshahi, S., Shoja-razavi, R. (2017). improving the thermal shock resistance of thermal barrier coatings through formation of an in situ YSZ/Al<sub>2</sub>O<sub>3</sub> composite via laser cladding. *J Mater Eng Perform*, vol. 26, no. 4, p. 1890–1899, DOI:10.1007/S11665-017-2591-0/tables/2.
- [25] Bumgardner, C., Croom, B., Li, X. (2017). High-temperature delamination mechanisms of thermal barrier coatings: In-situ digital image correlation and finite element analyses. *Acta Mater*, vol. 128, p. 54–63, DOI:10.1016/J.actamat.2017.01.061.
- [26] Feng, Y., Dong, T., Li, G., Wang, R., Ma, G.Z., Zhao, X., Liu, Q. (2020). The roles of stress in the thermal shock failure of YSZ TBCs before and after laser remelting. *J Alloys Compd*, vol.

- 828, p. 154417, DOI: 10.1016/j.jallcom.2020.154417.
- [27] Ghasemi, R., Shoja-Razavi, R., Mozafarinia, R., Jamali, H. (2013). Laser glazing of plasma-sprayed nanostructured yttria stabilized zirconia thermal barrier coatings. *Ceram Int*, vol. 39, no. 8, p. 9483–9490, DOI:10.1016/j.ceramint.2013.05.066.
- [28] Guo, L., Xin, H., Zhang, Z., Zhang, X., Ye, F. (2020). Microstructure modification of  $Y_2O_3$  stabilized  $ZrO_2$  thermal barrier coatings by laser glazing and the effects on the hot corrosion resistance. *Journal of Advanced Ceramics*, vol. 9, no. 2, p. 232–242, DOI: 10.1007/S40145-020-0363-Z.
- [29] Varghese, P., Vetrivendan, E., Vaishnavi Krupa, B.R., Shukla, P.K., Gupta, R.K., Rao, E.H., Puppala, G., Ningshen, S. (2021). Molten sodium corrosion of laser surface remelted yttria-stabilized zirconia thermal barrier coatings. *Corros Sci*, vol. 191, p. 109740, DOI:10.1016/j.corsci.2021.10974.
- [30] Mileşan, M., Gîrdu, C. C., Cîrtînă, L., Rădulescu, C. (2020). Mathematical modelling study of Hardox400 steel parts' roughness and hardness, cut with  $CO_2$  laser. *Strojniški Vestnik/Journal of Mechanical Engineering*, vol. 66, no. 2, p. 127–141, DOI:10.5545/sv-jme.2019.6320.
- [31] Lee, J. H., Tsai, P. C., Chang, C. L. (2008). Microstructure and thermal cyclic performance of laser-glazed plasma-sprayed ceria-yttria-stabilized zirconia thermal barrier coatings. *Surf Coat Technol*, vol. 202, no. 22–23, p. 5607–5612, DOI:10.1016/j.surfcoat.2008.06.118.
- [32] Tsai, P. C., Lee, J. H., Hsu, C. S. (2007). Hot corrosion behavior of laser-glazed plasma-sprayed yttria-stabilized zirconia thermal barrier coatings in the presence of  $V_2O_5$ . *Surf Coat Technol*, vol. 201, no. 9-11, p. 5143–5147, DOI:10.1016/j.surfcoat.2006.07.018.
- [33] Jasim M. K. (2011). Laser sealing of zirconia–yttria–alumina plasma sprayed coating. *Journal of King Saud University - Engineering Sciences*, no.1, p. 11–20, 2011, DOI:10.1016/j.jksues.2011.10.004.
- [34] Yilbas, B. S. (2015). Laser treatment of zirconia surface for improved surface hydrophobicity. *J Alloys Compd*, vol. 625, p. 208–215, DOI:10.1016/j.jallcom.2014.11.069.
- [35] Ahmadi-Pidani, R., Shoja-Razavi, R., Mozafarinia, R., Jamali, H. (2012). Improving the thermal shock resistance of plasma sprayed CYSZ thermal barrier coatings by laser surface modification. *Opt Lasers Eng*, vol. 50, no. 5, p. 780–786, DOI:10.1016/j.optlaseng.2011.12.007.
- [36] Gok M. G., Goller, G. (2015). Microstructural evaluation of laser remelted gadolinium zirconate thermal barrier coatings. *Surf Coat Technol*, vol. 276, p. 202–209, DOI:10.1016/j.surfcoat.2015.06.074.
- [37] Hegab, A., Dahuwa, K., Islam, R., Cairns, A., Khurana, A., Shrestha, S., Francis, R. (2021). Plasma electrolytic oxidation thermal barrier coating for reduced heat losses in IC engines. *Appl Therm Eng*, vol. 196, p. 117316, DOI:10.1016/j.applthermaleng.2021.117316.
- [38] Kumar D., Pandey, K. N. (2015). Optimization of the process parameters in generic thermal barrier coatings using the Taguchi method and grey relational analysis. *Composite Part L*, vol. 231, no. 7, p. 600–610, DOI:10.1177/1464420715602727.
- [39] Batista, C., Portinha, A., Ribeiro, R. M., Teixeira, V., Costa, M. F., Oliveira, C. R. (2005). Surface laser-glazing of plasma-sprayed thermal barrier coatings. *Appl Surf Sci*, vol. 247, no. 1–4, p. 313–319, DOI:10.1016/j.apsusc.2005.01.047.
- [40] Avci, A., Eker, A.A., Karabas, M. (2020). An investigation of oxidation, hot corrosion, and thermal shock behavior of atmospheric plasma-sprayed  $YSZ-Al_2O_3$  composite thermal barrier coatings. *International Journal of Materials Research*, vol. 111, no. 7, p. 567–580, DOI:10.3139/146.111920/.
- [41] Ahmadi-Pidani, R., Shoja-Razavi, R., Mozafarinia, R., Jamali, H. (2013). Laser surface modification of plasma sprayed CYSZ thermal barrier coatings. *Ceram Int*, vol. 39, no. 3, p. 2473–2480, DOI: 10.1016/j.ceramint.2012.09.005.
- [42] Evans, A. G., Charles, E. A. (1976). Fracture Toughness Determinations by Indentation. *Journal of the American Ceramic Society*, vol. 59, no. 7–8, p. 371–372, DOI:10.1111/J.1151-2916.1976.TB10991.X.
- [43] Batista, C., Portinha, A., Ribeiro, R. M., Teixeira, V., Oliveira, C.R. (2006). Evaluation of laser-glazed plasma-sprayed thermal barrier coatings under high temperature exposure to

- molten salts. *Surf Coat Technol*, vol. 200, no. 24, p. 6783–6791, DOI:10.1016/j.surfcoat.2005.10.011.
- [44] Garvie R. C., Nicholson, P.S. (1972). Phase Analysis in Zirconia Systems. *Journal of the American Ceramic Society*, vol. 55, no. 6, p. 303–305, DOI: 10.1111/J.1151-2916.1972.TB11290.X.
- [45] Tillmann W., Momeni, S. (2015). Influence of in-situ and postannealing technique on tribological performance of NiTi SMA thin films. *Surf Coat Technol*, vol. 276, p. 286–295, DOI:10.1016/j.surfcoat.2015.07.012.
- [46] Ahmadi-Pidani, R., Shoja-Razavi, R., Mozafarinia, R., Jamali, H. (2014). Improving the hot corrosion resistance of plasma sprayed ceria–yttria stabilized zirconia thermal barrier coatings by laser surface treatment. *Mater Des*, vol. 57, p. 336–341, DOI:10.1016/j.matdes.2013.12.075.
- [47] Pakseresht, A. H., Kimiayi, A., Alizadeh, M., Nuranian, H., Faeghinia, A. (2020). Microstructural study and hot corrosion behavior of bimodal thermal barrier coatings under laser heat treatment. *Ceram Int*, vol. 46, no. 11, p. 19217–19227, Aug. 2020, DOI: 10.1016/j.ceramint.2020.04.259.
- [48] Guo, L., Li, G., Gan, Z. (2020). Effects of surface roughness on CMAS corrosion behavior for thermal barrier coating applications. *Journal of Advanced Ceramics*, vol. 10, no. 3, p. 472–481, DOI: 10.1007/S40145-020-0449-7.
- [49] Wang, D., Tian, Z., Shen, L., Liu, Z., Huang, Y. (2014). Effects of laser remelting on microstructure and solid particle erosion characteristics of  $ZrO_2$ -7wt% $Y_2O_3$  thermal barrier coating prepared by plasma spraying. *Ceram Int*, vol. 40, no. 6, p. 8791–8799, DOI: 10.1016/j.ceramint.2014.01.101.
- [50] Fan, Z., Duan, W., Zhang, X., Mei, X., Wang, W., Cui, J. (2019). Influence of Preheating on the Microstructure Evolution of Laser Remelting Thermal Barrier Coatings/Ni-Based Single Crystal Superalloy Multilayer System. *Materials*, vol. 12, no. 19, DOI: 10.3390/MA12193088.
- [51] Kadam, N. R., Karthikeyan, G., Kulkarni, D. M. (2021). The effect of spray angle on the microstructural and mechanical properties of plasma sprayed 8YSZ thermal barrier coatings. *Journal of Micromanufacturing*, vol. 5, no.2, p.181-192, DOI:10.1177/25165984211016323.
- [52] J. D. Osorio, A. Lopera-Valle, A. Toro, and J. P. Hernández-Ortiz, "Phase transformations in air plasma-sprayed yttria-stabilized zirconia thermal barrier coatings," *Dyna (Medellin)*, vol. 81, no. 185, pp. 13–18, 2014, doi: 10.15446/dyna.v81n185.33409.
- [53] Girolamo, G., Blasi, C., Pagnotta, L., Schioppa, M. (2010). Phase evolution and thermophysical properties of plasma sprayed thick zirconia coatings after annealing. *Ceram Int*, vol. 36, no. 8, p. 2273–2280, DOI:10.1016/j.ceramint.2010.07.035.
- [54] Ilavsky, J., Stalick, J. K. (2000). Phase composition and its changes during annealing of plasma-sprayed YSZ. *Surf Coat Technol*, vol. 127, no. 2–3, p. 120–129, DOI: 10.1016/S0257-8972(00)00562-4.

## 7. APPENDIX

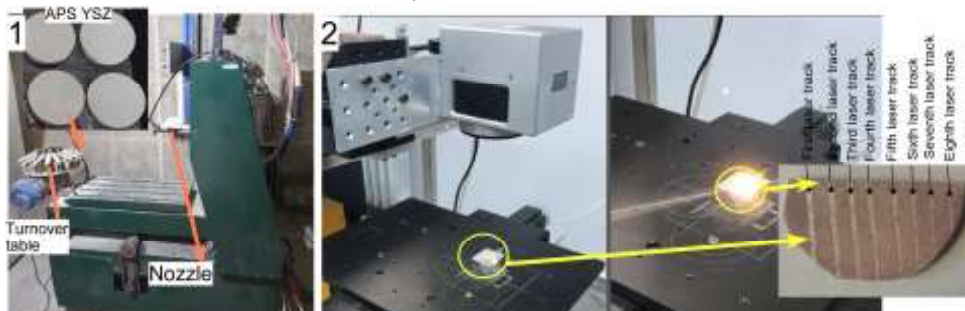


Fig. 8. a) Atmospheric plasma spray picture, b) CO2 laser glazing pictures